Received: 10 August 2022 | Revised: 18 October 2022 | Accepted: 18 November 2022

DOI: 10.1111/jace.18910

Journal of the American Ceramic Society

RESEARCH ARTICLE

Facile preparation of electrodes based on WO_3 nanostructures modified with C and S used as anode materials for Li-ion batteries

Gemma Roselló-Márquez | **Dionisio Miguel García-García** | **Mireia Cifre-Herrando** | **Encarna Blasco-Tamarit** | **José García-Antón**

Ingeniería Electroquímica y Corrosión, Instituto Universitario de Seguridad Industrial, Radiofísica y Medioambiental, Universitat Politècnica de València, Valencia, Spain

Correspondence
José García-Antón, Ingeniería Electroquímica y Corrosión, Instituto Universitario de Seguridad Industrial, Radiofísica y Medioambiental, Universitat Politècnica de València, C/Camino de Vera s/n, 46022 Valencia, Spain.
Email: jgarciaa@iqn.upv.es

Funding information
UPV for the concession of a postdoctoral, Grant/Award Number: PAID-10-21; Ministerio de Universidades for the concession of the predoctoral, Grant/Award Number: FPU19/02466; Comunitat Valenciana, Grant/Award Number: IDIFEDER/18/044

Abstract

An appropriate morphological and structure matrix configuration where lithium ions could insert and de-insert is essential for lithium-ion batteries (LiB). Tungsten oxides (WO_3) are especially attractive materials for this aim. In this research, the effects of the morphology and composition of WO_3 nanostructures on the charge/discharge behavior for Li-ion batteries are methodically examined. On the one hand, nanostructured WO_3 thin film was effectively synthesized by an electrochemical procedure. Then, an annealing treatment at 600°C in air environment for 4 h was carried out. In the second electrode synthesized, a carbon layer was uniformly deposited on WO_3 nanostructures to obtain a WO_3/C electrode. Finally, WO_3/WS_2 electrodes were prepared by means of in situ sulfurization of WO_3 one-step solid-state synthesis using tungsten trioxide (WO_3) and thiourea as precursor material. By using X-ray photoelectron spectroscopy, X-ray diffraction analysis, transmission electron microscopy, Raman spectra, and field-emission scanning electron microscopy, the three electrodes have been morphologically characterized. Electrochemical properties were analyzed by cyclic voltammogram, galvanostatic charge/discharge cycling, and electrochemical impedance spectroscopy. Among all the synthesized samples, WO_3/C nanostructures reveal the best performance as they exhibit the greatest discharge capacity and cycle performance (820 mA h g^{-1}).

KEYWORDS
charge/discharge curves, capacity, electrochemical properties, Li-ion batteries, WO3 nanostructures

1 | INTRODUCTION

Nowadays, the energy issue has become the greatest challenge and has drawn global interest in current society. Thanks to their great energy density and excellent cycle stability, lithium-ion batteries (LiBs) have attracted significant attention due to their multiple uses as mobile devices or power sources for electric vehicles.[1] Recently, much effort has been devoted to finding different anodic materials to substitute conventional ones in LiBs, and several transition metal oxides have been studied and considered alternative electrodes materials.[2,3]

There are three different groups of mechanisms during the LiBs performance: the insertion-extraction mechanism, alloying–dealloying process, and conversion reaction. The first mechanism refers to the ability of metal oxides with a multidimensional shell structure to insert lithium ions into their lattice without changing their crystalline structure.[4] Regrettably, just a little amount of these ions can be reversibly intercalated in this type of material; therefore, their specific capacity is reduced. The alloy–dealloy mechanism refers to the following equation[5,6]:

$$MO_x + Li \rightarrow Li_yM + Li_2O \quad (1)$$

in which the material (M) could produce a lithium alloy. The mechanism of lithium dealloying usually happens at low potentials (below 1.0 V vs. Li^+/Li) and shows high-capacity performance but disappears heavily through the charge–discharge procedure. Regarding the conversion reaction, in order to take advantage of the conversion reaction potentials, it must be treated before the appearance of problems such as (1) poor kinetics resulting in high polarization and thus poor energy efficiency, (2) poor capacity retention during the cycle, (3) higher potentials, and thus lower cell voltage unless combined with higher voltage electrode, (4) irreversible capacity loss in the first cycle, (5) finding chemical ways to reduce its range voltage reactivity toward Li, (6) marked hysteresis in the voltage between charge and discharge test, and (7) low coulombic efficiency.[7] For this, the use of metal oxides materials is a good option as it has a greater theoretical capacity than commercially available graphite. Nevertheless, structural instability and weak electrical conductivity are drawbacks that need to be improved.[8,9]

Tungsten oxide (WO_3) is an n-type semiconductor that possesses high electrochemical stability and has been analyzed in depth for its uses in electrochromic devices, photocatalysts, gas sensors, and as a producer of clean energy. Nevertheless, the use of WO_3 as anode material for batteries has attracted research interest recently.[10,11] Materials based on tungsten (WO_2, WO_3, $WO_3 \cdot H_2O$, etc.) have been studied as encouraging electrodes due to their high electronic conductivity ($10–10^{-6}$ S cm^{-1}),[12] excellent intrinsic density (>7 g cm^{-3}), small radius, correct crystal phase for rapid ion insertion, and exceptional electrochemical behavior.[13–15]

However, the structure of WO_3 will be modified during the charge/discharge reactions, which will cause a worsening of electron diffusion between the anodic material and the matrix, reducing the electrode cycle stability. To deal with these difficulties, carbon has been used to form a composite material.[16,17]

Combined electrodes composed by coupling metal oxides and conductive carbon material can result in new electrodes with the advantages of both components. This has been the case for the WO_3 with a carbon coating which has exceptional electrical, thermal, mechanical, and optical properties and an improvement of the electron transport rate.[18,19] Some published works have investigated the possible improvements of these new combined electrodes in different environmental and energy applications.[20,21]

Moreover, S has been incorporated into the nanostructures of WO_3 in the form of WS_2 due to their extraordinary mechanical, electrical, and optical properties. WS_2 is a material known for having a similar structure to graphene, that is, a layered structure with a plane of metal atoms between two planes of chalcogen atoms.[22,23] This material has strong covalent bonds in the S–W–S layer and weak van der Waals forces between those layers, leading to an efficient insertion and extraction of lithium ions, as has been shown in some research work.[9,24,25]

In this investigation, a simple process is used to synthesize crystalline WO_3 nanostructures with a well-defined morphology through an electrochemical procedure known as electrochemical anodization, which has several advantages such as being a simple and economical procedure, its parameters being easy to control, and obtaining high surface/volume ratio nanostructures.

In addition, in this study, we synthesized carbon-layered WO_3 nanostructures (WO_3/C) using an evaporation-based method and WO_3/WS_2 nanostructures by means of in situ sulfurization. To analyze the influence of carbon and sulfur, the morphological and structural properties of the compounds prepared were evaluated by means of several techniques: field-emission scanning electron microscopy (FE-SEM), transmission electron microscopy (TEM), X-ray diffraction (XRD), X-ray photoelectron spectroscopy (XPS), and Raman spectroscopy. Meanwhile, the electrochemical properties of the samples with a bilayer structure were investigated using cyclic voltammetry (CV), charge–discharge cycles, and electrochemical impedance spectroscopy (EIS).

2 | EXPERIMENTAL DETAILS

2.1 | WO_3 and WO_3/C nanostructures synthesis

All the chemical compounds employed possessed an analytical grade and were acquired from Panreac. The pure WO_3 nanostructures were synthesized using the electrochemical anodization method using CH_4O_3S as an electrolyte. The detail of the preparation process could be found in our previous work.[26] After the anodization, a thin blue layer was formed, and it was annealed at 600°C for 4 h in air to obtain a crystalline structure.

In order to prepare the WO_3/C electrodes, an evaporation method was chosen. This method consists in applying 8 V and vacuum pressure until reaching 10^{-5} mbar using the LEICA MED 20 equipment on the WO_3 nanostructures previously synthesized, as specified in our work.[26]

Finally, a solid-state synthesis was used to prepare the WO_3/WS_2 electrodes from basic WO_3 nanostructures. The WS_2 layer was obtained by heating tungsten oxide nanostructures in the presence of thiourea with a WO_3/thiourea ratio of 1:48 during 3 h at 773 K under argon. Once these 3 h had elapsed, the nanostructures were cooled to room temperature in an inert atmosphere, resulting in a black product. The chemical reaction is shown in the following equation[27]:

$$2WO_3 + 3CH_4N_2S \rightarrow WO_3WS_2 + 4NH_3 + 3CO + N_2 \quad (2)$$

After the annealing treatment, the nanostructures were used in Li-ion batteries as an anode.

2.2 | Structure characterization

The nanostructures' morphology and the size of each sample were analyzed by employing an FE-SEM (Zeiss Ultra 55) and high-resolution TEM (HRTEM, JEOL, JEM 2100F). The crystal structure was examined by XRD (Bruker D8 Advance) with Cu K_α radiation (λ = 1.5406 Å) at a scan rate of 10° min^{-1}. Raman spectroscopy was performed in a range of 0–2000 cm^{-1} on a WITec alpha300 R confocal Raman microscope.

The electronic structure and the chemical state of the elements that exist in the samples were analyzed by XPS. The K-Alpha Thermo Scientific system with an Al-K_α radiation (1486.6 eV) was used to obtain the composition data. The pass energy and the pressure were 50 eV and 10^{-7} Torr, respectively.

2.3 | Electrochemical tests

The electrochemical analyses were realized with a two-electrode cell configuration. These batteries were setup by using the WO_3 nanostructures layers as the working electrode (the mass of active material used in each battery was 6.5 mg). The counter electrode used in this test was a lithium sheet. The solution used as an electrolyte (Merck) was 1 M $LiPF_6$ in a nonaqueous solution of dimethyl carbonate, and ethylene carbonate with a volume relation of 1:1 and fiberglass were used as spacers. The cells were constructed in a glove box with an inert atmosphere, and the electrolyte volume incorporated in each battery was 300 μl. Charge–discharge experiments were carried out with an Autolab PGSTAT302N potentiostat. The range potential between the charge and discharge tests that have been carried out was 0.01–4 V versus Li/Li^+ at a current density of 100 mA g^{-1}. The cyclic voltammogram (CV) measurements were performed at a scan rate of 0.5 mV s^{-1} of between 0.01 and 4.0 V on an Autolab PGSTAT302N potentiostat.

The EIS was examined at open circuit potential. The frequency range used was 0.1–10 kHz, and the signal perturbation had an amplitude of 10 mV.

3 | RESULTS AND DISCUSSION

3.1 | FE-SEM and TEM

The structure and morphology of the electrodes were analyzed using FE-SEM and TEM. As seen in Figure 1, each electrode contains homogeneous and tiny nanostructures. As shown in Figure 1A, the WO_3 nanostructures exhibit a rounded morphology, and it can be seen that these nanorods look longer and thinner in contrast with the other nanostructures.

Furthermore, the FE-SEM images show that the carbon-coating procedure does not generate any substantial structural or morphological changes to the WO_3/C samples (Figure 1B). Besides, the WO_3 nanostructures subjected to carbon coating show a spongy layer morphology containing a rough surface.

Finally, in the case of WO_3/WS_2, when the nanostructures were put through the in situ sulfurization process, the synthesized nanostructures show a more different morphology than the previous ones. The WO_3/WS_2 electrode becomes more irregular than the two other samples, with internetworked macro and mesopores due to the sulfur and carbon deposited, as seen in Figure 1C.

In addition, an EDX analysis of each electrode was performed, obtaining their composition and verifying the presence of the principal elements in the nanostructures.

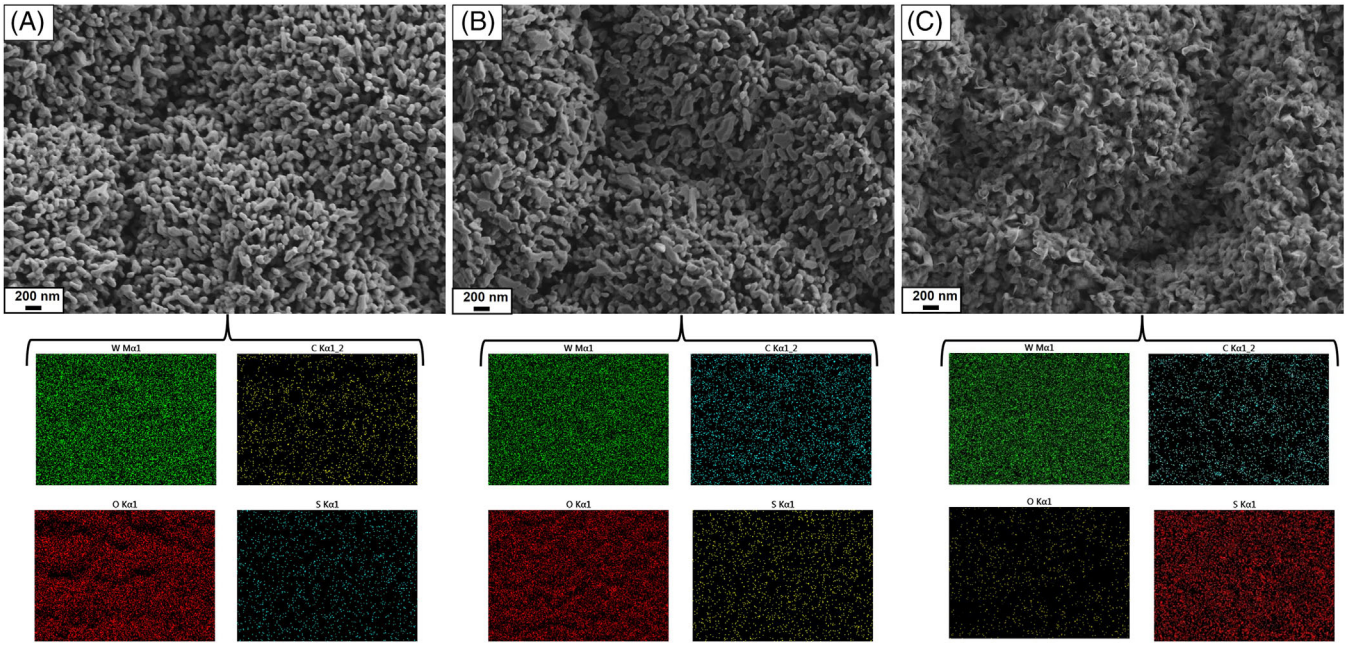

FIGURE 1 Field-emission scanning electron microscopy (FE-SEM) images at 20 000× and EDX mapping of the surface of (A) WO_3, (B) WO_3/C, and (C) WO_3/WS_2

TABLE 1 EDX composition of each sample

	WO_3		WO_3/C		WO_3/WS_2	
Element	**wt%**	**at%**	**wt%**	**at%**	**wt%**	**at%**
C	0.13	0.78	2.08	11.02	2.4	14.29
N	0.07	0.33	0.09	0.39	1.62	8.29
O	15.14	74.54	15.08	66.32	0.35	1.58
S	0	0	0	0	22.96	51.77
W	65.66	24.35	61.75	22.27	63.67	24.07
Total:	100	100	100	100	100	100

Table 1 shows each composition, where it can be seen that the WO_3/C and WO_3/WS_2 electrodes have a greater amount of carbon than the WO_3 one due to carbon (2 wt%) and thiourea coating (2.4 wt%), respectively. Moreover, regarding sulfur analysis, in the case of the WO_3/WS_2 electrode, a greater amount of sulfur, as opposed to oxygen, has been detected, so it can be said that a large part of the WO_3 has become WS_2. This statement will be corroborated with XRD and XPS results.

Finally, EDX mapping is shown also in Figure 1. In all cases, it illustrates that the elements of W, O, and C are distributed homogeneously on the surface. Moreover, in the WO_3/WS_2 electrode, it can be checked that the presence of S is higher than in the other samples but is spread homogeneously too, indicating the coexistence of WO_3 and WS_2.

As proof that the deposition of the sulfur has been superficial, in Figure 2, an EDX analysis of a nanostructure of the inner layers obtained by scratching the surface is shown. There it can be seen that the nanostructures of the deeper layers have a composition of WO_3, without the presence of S, indicating that the coating has been superficial.

TEM images of the three electrodes are shown in Figure 3, revealing that the samples comprise nano-sized structures. Figure 3A,B confirms that the size and morphology of the samples (WO_3 and WO_3/C, respectively) are similar, as seen in the FE-SEM images. Figure 3G presents the WO_3 HRTEM image, where it can be seen that WO_3 nanostructures possess interplanar distances of 0.33 and 0.36 nm, associated with the (1 0 1) and (0 0 1) crystal lattice planes, respectively,.[28–30] Figure 3H shows the distances between the planes of the WO_3/C electrode. The determined lattice fringe with an interplanar spacing of 0.39 nm (Figure 3H) refers to the (1 1 0) plane.[10,31] This crystallographic plane is characterized by offering excellent electronic contact between the nanorods, thus

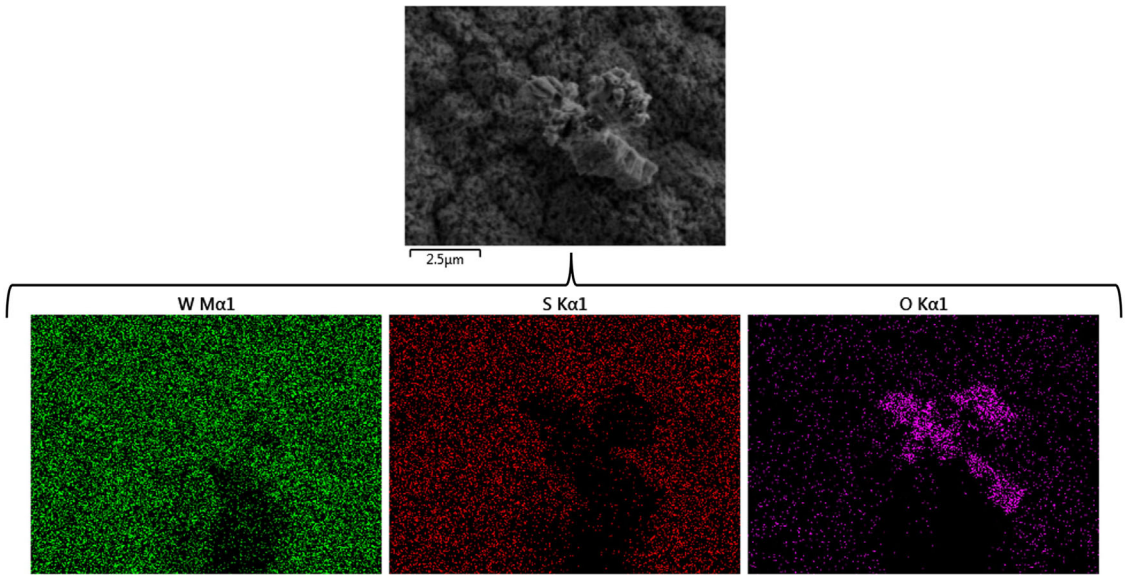

FIGURE 2 Field-emission scanning electron microscopy (FE-SEM) images at 20 000× and EDX mapping of the surface of the WO_3/WS_2 nanostructure

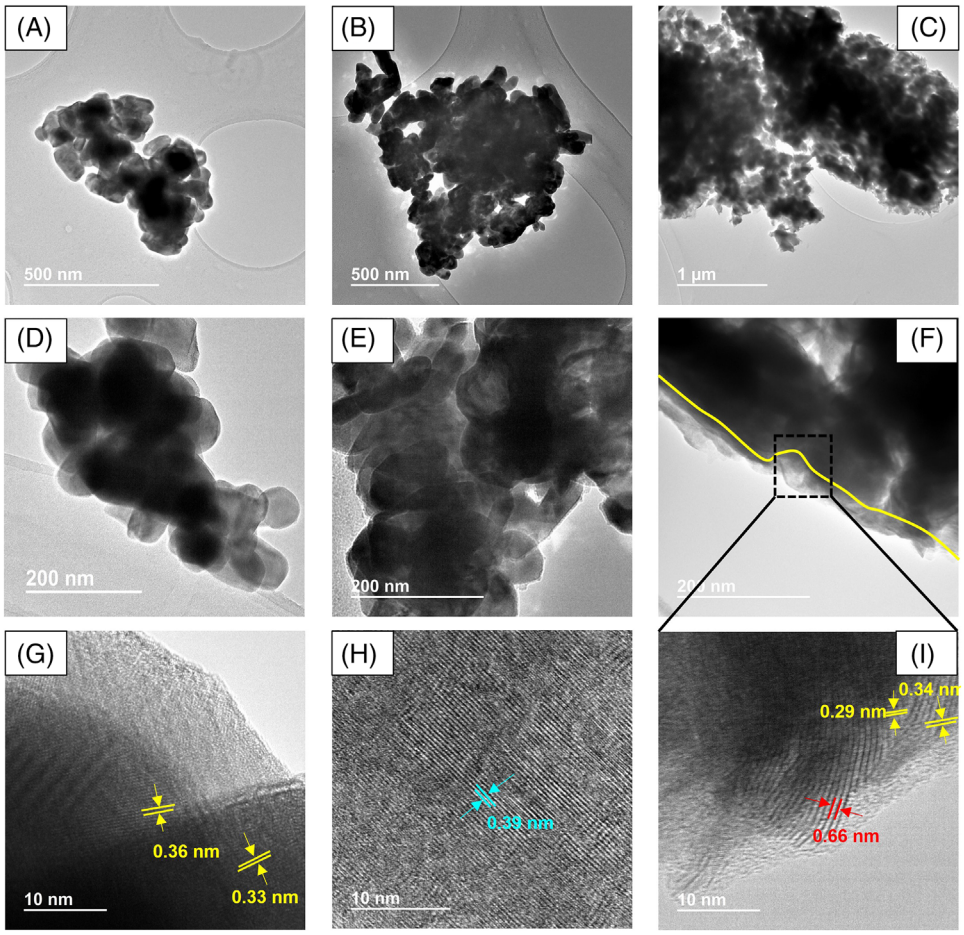

FIGURE 3 High-resolution transmission electron microscopy (HR-TEM) images at different magnifications of (A), (D), and (G) WO_3, (B), (E), and (H) WO_3/C, and (C), (F), and (I) WO_3/WS_2

reducing the resistance between the grain interfaces. Moreover, such a tiny nanostructure size can successfully hold the movement of lithium ions and electrolytes during charging/discharging performance.[32]

In addition, Figure 3C shows a TEM image of the WO_3/WS_2 sample. In this picture, an ultrathin WS_2 layer homogeneously anchored on the WO_3 surface can be observed. As demonstrated in Figure 3F, an obvious interface between WO_3 and WS_2 was seen, suggesting that the sulfurization of WO_3 had been carried out superficially. The distances between lattice fringes are 0.29 and 0.34 nm, corresponding to the (0 2 2) and (2 0 0) planes for WO_3, respectively.[5,16] However, the lattice fringes' spacing of WO_3/WS_2 is 0.66 nm, which is related to the (0 0 2) plane of WS_2.[33,34] Therefore, WS_2 was developed from the sulfurization of the (0 2 2) plane of WO_3 and the sulfurization of an exhibit low-indexed facet like (2 0 0) of the WO_3 nanocrystal.[9,35]

3.2 | XPS

To investigate the composition and the chemical states of the elements present in the samples in more depth, XPS measurements were performed. It is known that tungsten can be present in different chemical states from 4+ to 6+ depending on the element with which it forms a bond, which can be oxygen, sulfur, and so on. Figure 4A–C displays the W 4f XPS spectra belonging to WO_3, WO_3/C, and WO_3/WS_2 samples. The W 4f spectra of WO_3 and WO_3/C electrodes show four peaks associated with two doublets with different intensities, suggesting that tungsten is found in two different oxidation states. The peaks at 35.58 and 34.47 eV were associated with W^{6+}, whereas the peaks at 36.58 and 37.68 eV belonged to W^{5+}.[2,36,37]

However, the W 4f spectrum of WO_3/WS_2 differs from the other two samples as the peaks appear shifted to the left. This is due to the tungsten valence changes from +6 to +4 when forming bonds with the sulfur to form WS_2. The peaks at 34.58 and 34.98 eV are assigned to the W^{6+} of WO_3, and the peaks found at 32.28 and 32.85 eV are attributed to the W^{4+} of WS_2.[8,25]

O 1s XPS spectra of WO_3 and WO_3/C (Figure 4D–E) show a predominant peak at 530.48 eV that is ascribed to the oxygen present on the lattice of the samples and O^{2-} bond with tungsten, whereas the shoulder at 531.1 eV is due to impurities such as carbonates or OH^- groups on the surface.[3] The peaks of the O 1s spectrum of WO_3/WS_2 arise at higher binding energies than those mentioned before, its area being smaller than the corresponding area of WO_3 and WO_3/C electrodes (as shown in Table 2).[15,38]

The C 1s XPS spectrum of WO_3/C and WO_3/WS_2 samples (seen Figure 4G,H) presents three peaks at 284.68, 285.88, and 287.08 eV for the WO_3/C sample and 284.68, 286.28, and 286.68 eV for the WO_3/WS_2 electrode. The second peak (at 285.88 eV in the WO_3/C sample) is associated with surface carbon deposited in the samples, and the minor C 1s (287.08 eV) peak and the second O 1s (532.28 eV) peak imply the existence of oxygen atoms bonded to carbon atoms to form compounds like carbonyl groups.[5,39] The peak is shown asymmetrically, indicating the presence of carbon bonds as sp^2 and sp^3. Moreover, the peak area of the WO_3/C sample is greater than the area corresponding to the WO_3/WS_2 sample (as shown in Table 2), indicating a higher amount of carbon on the surface, which means that the interfacial resistance of the electrode will decrease, producing improved electrochemical performance.[40]

Finally, in the WO_3/WS_2 sample, two different peaks can be observed in the spectrum of S 2p. These peaks confirm the existence of WS_2 in the electrodes (Figure 4I) as the peaks situated at 163.6 and 162.4 eV correspond to the S–W bond.[25]

3.3 | XRD

The crystal structures of each sample were studied by XRD. Figure 5 shows the XRD patterns of WO_3, WO_3/C, and WO_3/WS_2 samples. The diffracted peaks of WO_3 and WO_3/C electrodes have a sharp shape, as is characteristic of nanostructures with high crystallinity. The peaks at 2θ values of 23.1°, 23.58°, 24.44°, 28.93°, 33.52°, 47.48°, 48.08°, 50.73°, 58.4°, and 75.5°can be indexed to (1 0 1), (0 2 2), (1 2 0), (1 1 0), (2 0 0), (2 2 2), (4 0 0), (1 1 4), (4 2 0), and (4 2 2) crystal planes of hexagonal WO_3 (JCPDS no. 83-0950).[18,41,42]

However, for WO_3/C nanostructures, the intensity of each peak clearly diminished with carbon content on the surface of WO_3. The reason of this diminution is the presence of a carbon layer on the electrode surface and its amorphous structure. Moreover, it can also be stated that the carbon coating procedure did not damage the composition of WO_3 as all the peaks observed in the WO_3 sample are also seen in the WO_3/C.[43,44]

Finally, after thiourea annealing treatment under argon atmosphere, the XRD pattern displays peaks of both WS_2 and WO_3. The characteristic peak associated with WS_2 is that which appears at 14.2° and corresponds to the (0 0 2) $h\,k\,l$ plane.[8,9] Moreover, the strong peaks at 23.54°, 33.52°, 48.14°, 48.08°, and 75.24° correspond to (0 2 2), (2 0 0), (4 0 0), and (4 2 2) $h\,k\,l$ planes of the hexagonal tungsten oxide phase. However, the peaks' intensity is decreased in this case, even totally disappearing, as is the case with the peaks corresponding to (1 0 1), (1 1 0), (2 2 2), and (1 1 4) crystal planes that have been totally diminished. This happens

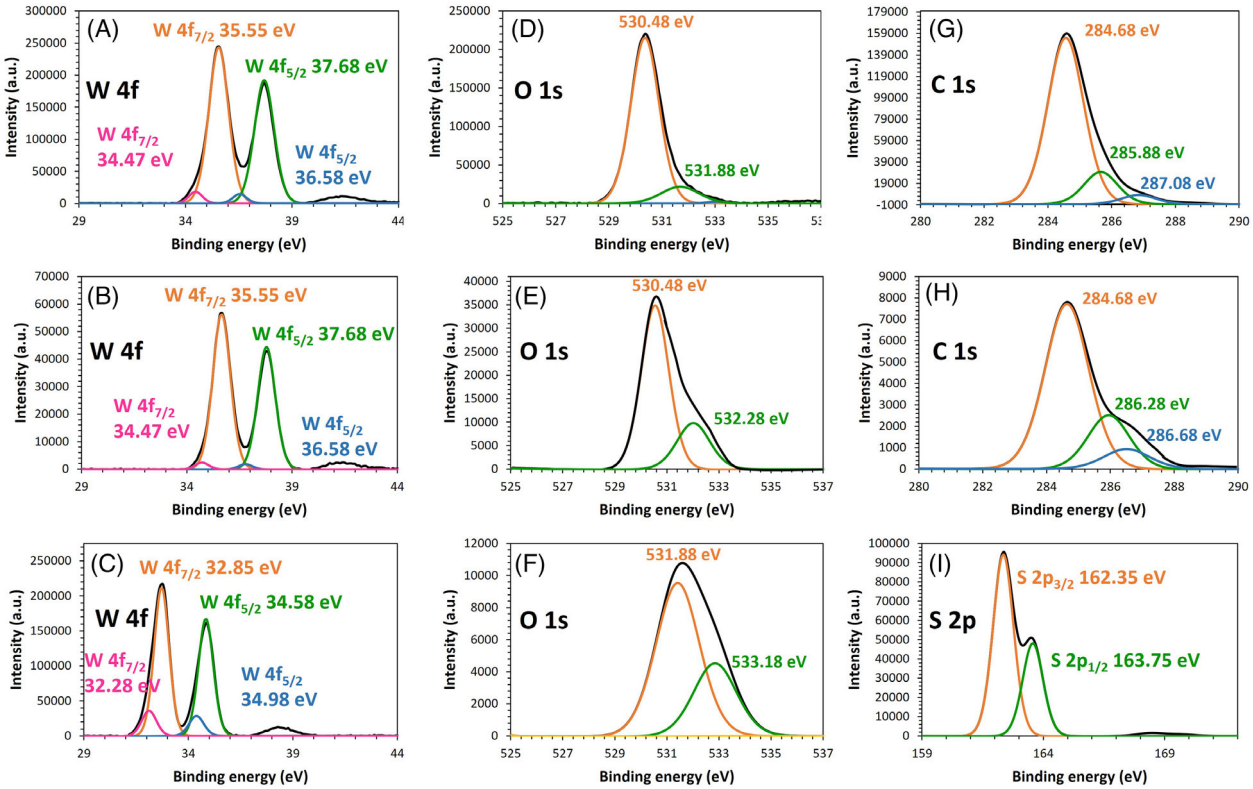

FIGURE 4 X-ray photoelectron spectroscopy (XPS) W 4f spectrum of (A) WO_3, (B) WO_3/C, (C) WO_3/WS_2. XPS O 1s spectrum of (D) WO_3, (E) WO_3/C, (F) WO_3/WS_2. XPS C 1s spectrum of (G) WO_3/C, (H) WO_3/WS_2. XPS S 2p spectrum of (I) WO_3/WS_2

TABLE 2 Peak table of WO_3, WO_3/C, and WO_3/WS_2 samples

	WO_3		WO_3/C		WO_3/WS_2	
	Peak BE	Area (counts)	Peak BE	Area (counts)	Peak BE	Area (counts)
W $4f_{7/2}$	35.58	286 912.29	35.65	60 336.4	32.85	192 837.35
W $4f_{5/2}$	37.68	15 222.9	37.68	1958.01	34.98	33 264.84
O 1s	530.48	293 158.46	530.48	47 648.36	531.88	20 453.28
O 1s	531.88	2573.01	532.28	42 769.54	533.18	9574.32
C 1s	–	–	284.68	224 689.53	284.68	19 747.67
C 1s	–	–	285.88	40 455.5	286.28	10 639.31
C 1s	–	–	287.08	11 691.22	286.68	24 499.48
S $2p_{3/2}$	–	–	–	–	162.35	102 259.9
S $2p_{1/2}$	–	–	–	–	163.75	2444.25

because the WO_3 concentration is lower than that of WS_2, the latter being the majority species.[39]

3.4 | Raman

Figure 6 shows the Raman spectrum of WO_3, WO_3/C, and WO_3/WS_2 electrodes, indicating that the spectra of all samples were similar and showed sharp peaks. Particularly, the most obvious common peaks are those that appear at 707 and 805 cm^{-1}, which were related to W–O stretching and bending modes, respectively. Furthermore, the peaks at 136.5, 260, and 328 cm^{-1} were also detected, corresponding to O–W–O bending modes, which belong to the crystalline tungsten oxide and the existence of oxygen vacancies. However, there are some differences between them.[13,14,45]

With the aim of confirming the presence of carbon in the WO_3/C sample, the Raman bands of carbon in this electrode were analyzed between 1000 and 2000 cm^{-1}. The

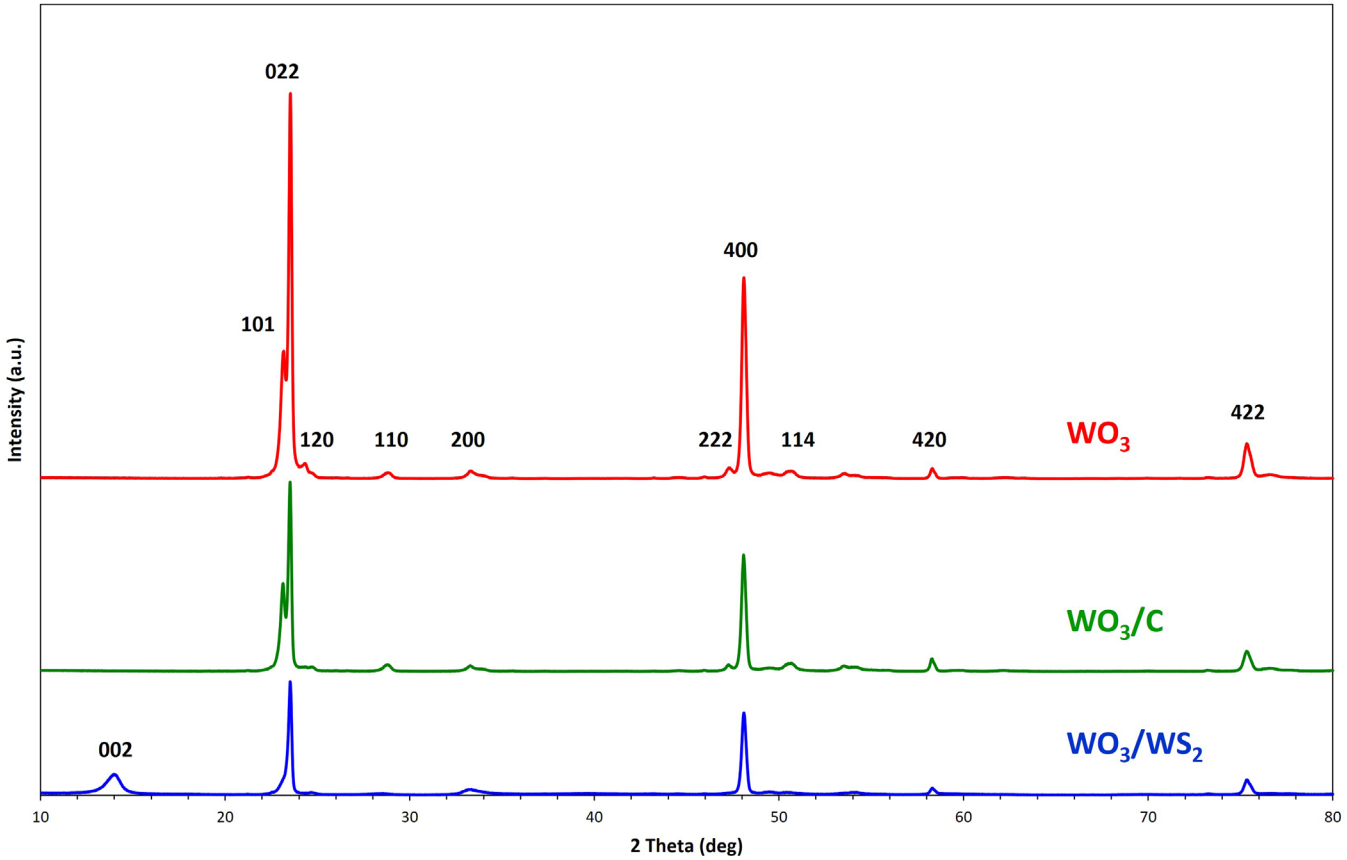

FIGURE 5 X-ray diffraction (XRD) spectra of WO_3, WO_3/C, and WO_3/WS_2 nanostructures

Raman peak was detected at 1574 cm^{-1}, which belongs to the E_{2g} phonon of C sp^2 atoms and to defects in graphitic carbons, showing a considerable amount of carbon in the electrode and, therefore, indicating the successful deposition of carbon on WO_3 nanostructures.[31,40]

In the WO_3/WS_2 Raman spectrum, the characteristic band of WS_2 was observed at 425 cm^{-1}, which also confirms that WS_2 in the crystalline phase was effectively obtained.[34] Moreover, the presence of carbon has also been detected in this electrode as a band at 1585 cm^{-1} has been detected.[27,33] However, vibration peaks of WO_3 in Raman spectroscopy are less pronounced in this sample, suggesting that a large amount of the WO_3 has become WS_2. Therefore, these results confirm the conclusions obtained with XRD tests.

3.5 | Electrochemical tests

3.5.1 | CV

To study the behavior of each sample (WO_3, WO_3/C, and W_2S/WO_3 nanostructures) as an anode in LiBs, electrochemical measurements were performed. To carry out these tests, two-electrode cells were manufactured with Li metal sheet as the counter electrode. The cyclic voltammograms (CV) of these three samples for the three initial cycles, between a potential range of 0–4 V and at a scan rate of 0.5 mV s^{-1}, are displayed in Figure 7A–C. From CV curves, it can be seen that there is a great variation between the first cycle and the following ones in the three samples analyzed. In the first electrode (WO_3, Figure 7A), two reduction peaks can be seen around 1.5 and 0.59 V, related to the electrochemical production of amorphous Li_2O (as shown in Equation 3), and the development of a partially irreversible solid electrolyte interphase (SEI) layer.[39] The disappearance of the cathodic peak at 0.59 V in the following cycles suggests that during the first cycle, an irreversible reaction of lithium insertion in the crystalline structure is taking place. This reaction produces an irrecoverable phase transformation, causing an irreversible capacity reduction.[46]

$$WO_3 + 6Li^+ + 6e^- \rightarrow W + 3Li_2O \quad (3)$$

In the anodic direction, one can observe a peak at 1.25 V, which indicates the formation of W^{6+} from W to obtain WO_3 (Equation4). In the two next cycles, this peak also

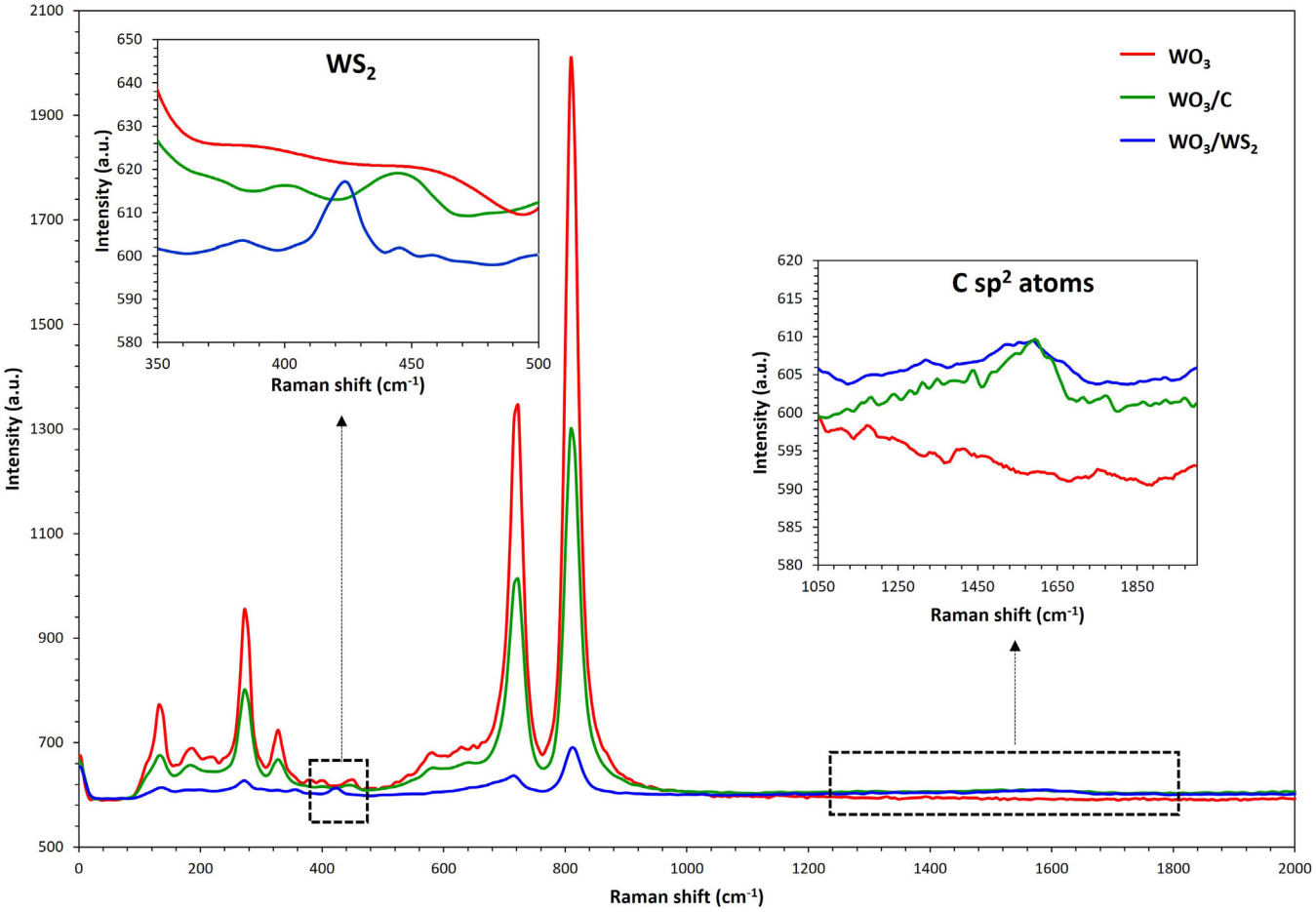

FIGURE 6 Raman spectra of WO_3, WO_3/C, and WO_3/WS_2 samples

appears, which denotes reversibility in the reactions and capacity stability.[30]

$$W + 3Li_2O \rightarrow WO_3 + 6Li^+ + 6e^- \quad (4)$$

So, the peaks that appear in the reduction direction at 0.59 and 1.5 V showed the lithium insertion reaction, whereas the peaks at 1.25 V revealed the lithium extraction process.

Comparing with the WO_3 sample, the peaks mentioned above are not observed in the different cycles of the WO_3/C electrode due to the greater presence of carbon in the nanostructures (Figure 7B). The presence of coated carbon has successfully decreased the anodic potential of the WO_3/C samples, which enhances the Li^+ ions reaction and improves the electronic conductivity. Therefore, the CV form of the WO_3/C sample shows its excellent cycle behavior.[45]

In the case of the W_2S/WO_3 sample (Figure 7C), cathodic peaks at 0.7 and 0.9 V appeared and were assigned to irreversible reactions produced by the existence of surface residual species that vanished in following cycles, revealing an elimination of these surface impurities. The peaks that appear at 1.5 and 1.9 V in the first cycle are related to the reversible collection of Li_2O compound (Equation 3) and a partially irreversible growth of a SEI layer. Regarding the anodic peaks, at 1.25 V a peak emerged in all cycles, indicating the oxidation reaction shown at Equation (4).[6,47]

3.5.2 | Charge/discharge curves

To prove the benefits of WO_3/C nanostructures, their anodic behavior was contrasted with WO_3 and WO_3/WS_2 electrodes with charge/discharge tests at a current density of 100 mA g^{-1}. Figure 8 illustrates the charge/discharge curves of each electrode.

Regarding the WO_3 electrode, a plateau at 1.4 V is observed in the first discharge curve, attributed to the development of W and Li_2O (Equation 3). Moreover, it could correspond to irreversible reactions between Li^+ ions and WO_3 nanostructures and the growth of an SEI layer. With these curves, it is also possible to find the

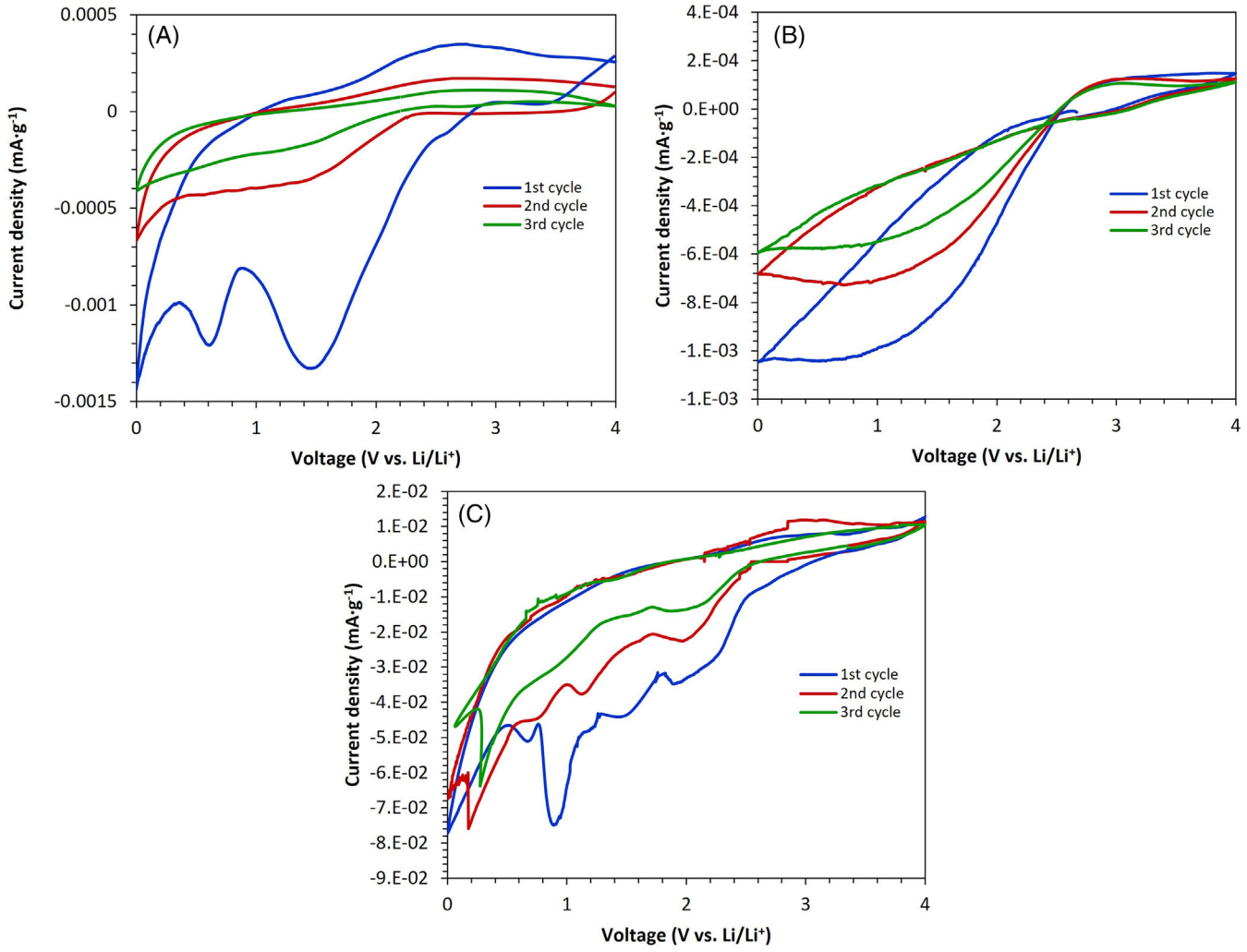

FIGURE 7 Cycle voltammograms curves of nanostructures based on (A) WO_3, (B) WO_3/C, and (C) WO_3/WS_2 in the voltage range of 0.01–4 V versus Li/Li^+ at a scan rate of 0.5 mV s^{-1}

specific charge and discharge capacities, which in this case are 170 and 335 mA h g^{-1}, respectively. These results may be caused by the weak electrical contact between grain boundaries.[48]

In WO_3/C nanostructures, the carbon layer improves the electrical contact and enhances the conductivity of the nanostructures. Moreover, during the electrochemical performance, it provides a greater charge transfer. Consequently, the charge–discharge curves become more stabilized and very smooth without any obvious oscillation, indicating a robust cycling stability.[31,44]

This electrode exhibited a discharge capacity of 820 mA h g^{-1} in the first cycle, whereas the initial charge capacity is 367 mA h g^{-1}. Due to the substantial number of defects and holes on the nanostructures' surface, the WO_3/C electrode shows this great specific capacity, which improves the storage and movement of Li^+ ions.

Finally, the effect of the WS_2 presence in the nanostructures improves their electrochemical performance compared to WO_3 electrode behavior as they possess a higher storage capacity. This capacity increase is because of the transport problems of electrons, and Li^+ ions are reduced and the conversion reaction of these is favored.[49,50]

So, the electrochemical behavior of WO_3/C nanostructures was better than that of WO_3/WS_2 and WO_3 electrodes, which was attributed to the smaller size of the nanostructures, a greater surface area and excellent diffusion on carbon surface. With all these properties, WO_3/C electrodes have a better Li^+ ion storage capacity, as well as a superior transfer performance, resulting in an improved cycling stability and better reversible capacity.[51]

Figure 9A shows the specific discharge capacities of WO_3, WO_3/C, and WO_3/WS_2 at a current density of 100 mA g^{-1} (voltage range = 0.01–4 V) for the first 50 cycles. The combined electrodes (WO_3/C and WO_3/WS_2 samples) show a high specific capacity and an exceptional stability compared to the basic WO_3 electrode.

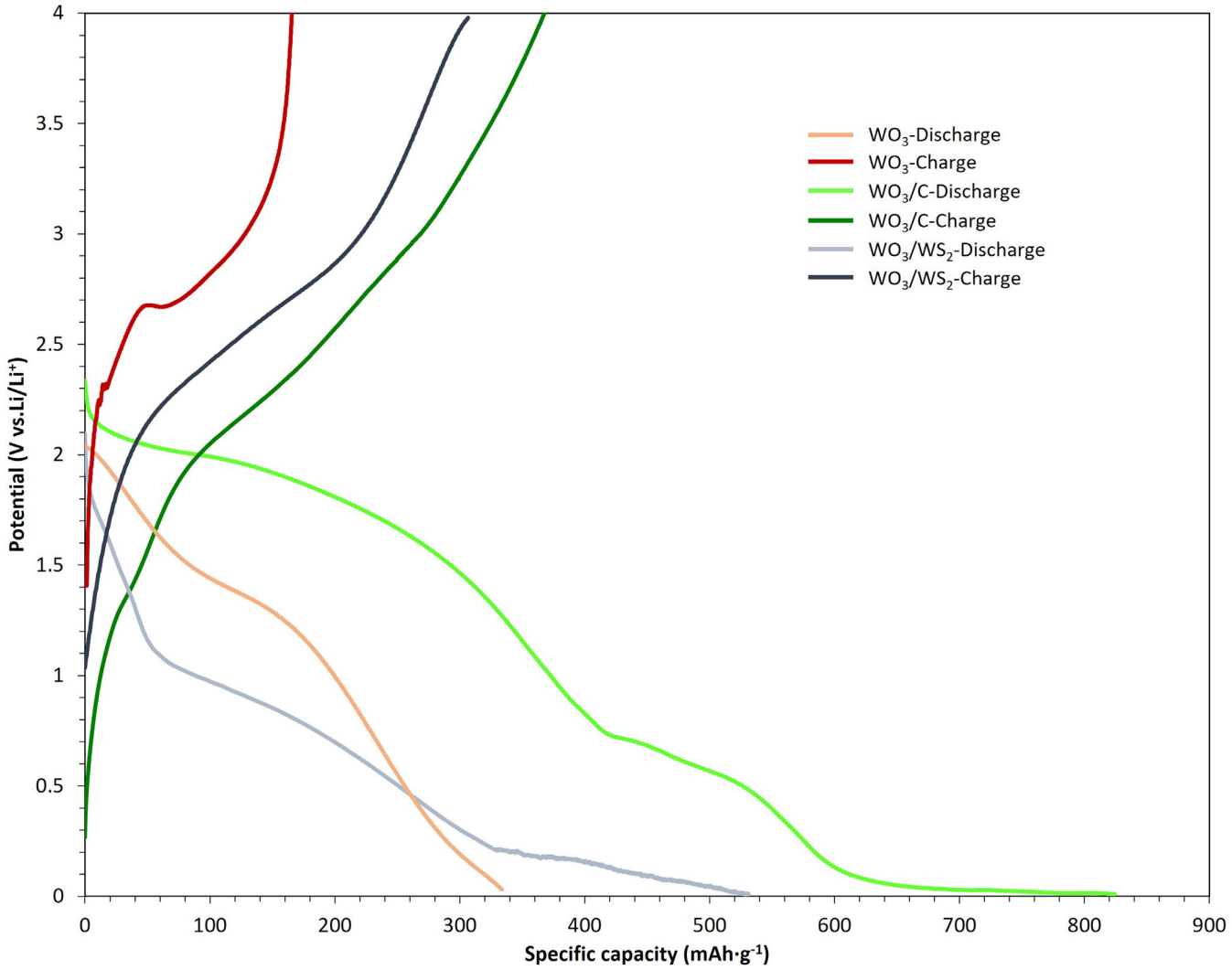

FIGURE 8 Charge/discharge curves of WO_3, WO_3/C, and WO_3/WS_2 in the 0.01–4 V versus Li/Li^+ range voltage at 100 mA g^{-1} current density

In the second cycle, the discharge capacities decreased to 199, 713, and 384 mA h g^{-1}, which are 40%, 13%, and 26%, respectively, of the first cycle capacities. After 50 cycles, the discharge capacity of the WO_3 electrode has decreased significantly and is equal to 91 mA h g^{-1}. In contrast, the discharge capacity of the WO_3/C electrode is 631 mA h g^{-1}, the decrease in discharge capacity being much smaller, which indicates a good cycling stability.

Moreover, in Figure 9A, the Coulombic efficiency is shown for each electrode during 50 cycles. This efficiency is higher and more stable in case of the WO_3/C electrode than for the rest of the samples. So, this behavior indicates an enhancement in reversible lithium storage and therefore a better performance as an anode in lithium-ion batteries.

In addition, an important criterion to be evaluated from the point of view of the applicability of the materials in lithium-ion batteries is the ability to withstand very high current rates. To do this, the rate capacity (Figure 9B) of the three electrodes has been discussed, as it is directly related to the current rate that they can resist. A high reversible capacity and an excellent cyclic behavior were only observed in the WO_3/C electrode.

The carbon coating plays a very important role in tremendously improving the rate capability of composite electrodes. It was tested over a wide range of discharge current densities: 0.1, 0.5, 0.7, 1, and 2 A g^{-1}. The specific capacities of the WO_3/C electrode are 750 mA h g^{-1} (0.1 A g^{-1}), 650 mA h g^{-1} (0.5 A g^{-1}), 620 mA h g^{-1} (0.7 A g^{-1}), 600 mA h g^{-1} (1 A g^{-1}), and 582 mA h g^{-1} (2 A g^{-1}).

However, the discharge capacity of the WO_3 electrode decreases significantly with increasing current rates. WO_3 capacities are 200 mA h g^{-1} (0.1 A g^{-1}), 120 mA h g^{-1} (0.5 A g^{-1}), 70 mA h g^{-1} (0.7 A g^{-1}), 29 mA h g^{-1} (1 A g^{-1}), and 10 mA h g^{-1} (2 A g^{-1}). These capacitances drop off

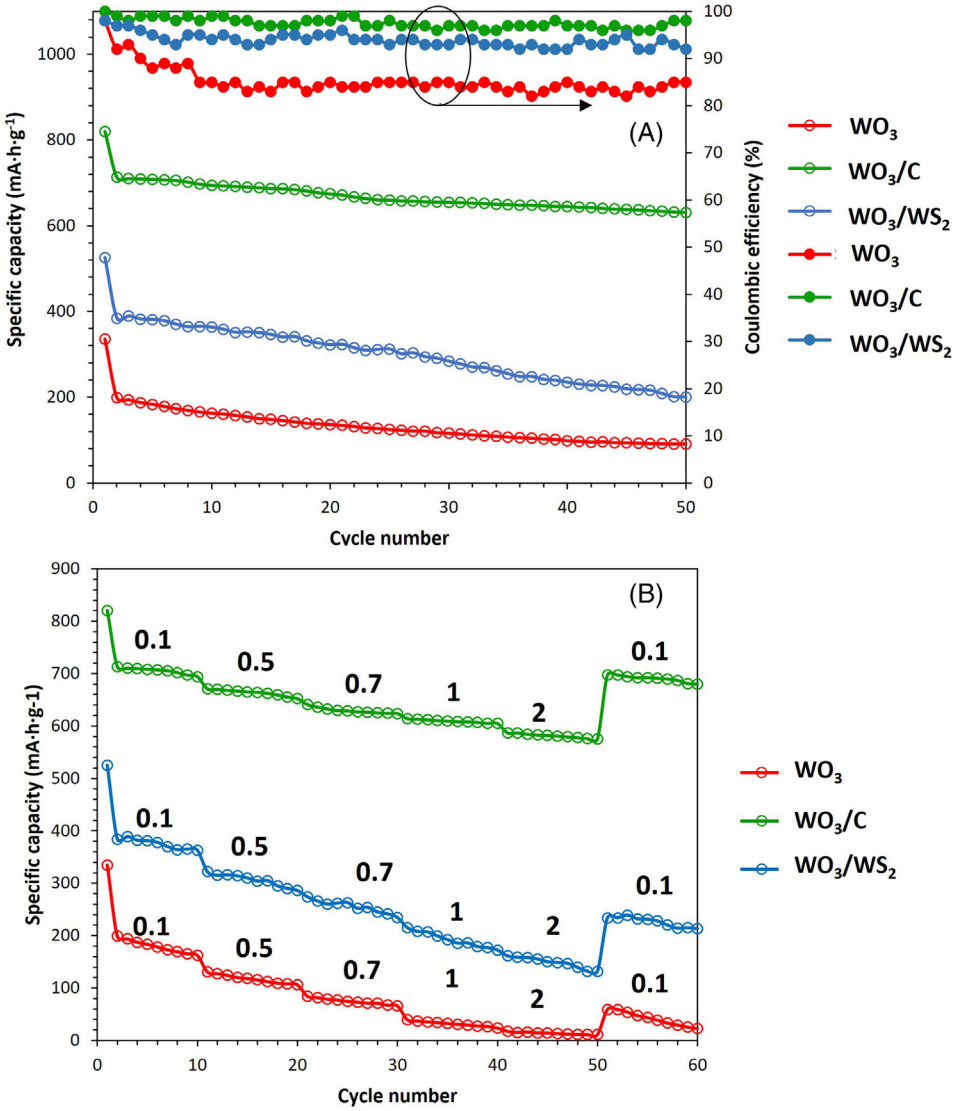

FIGURE 9 (A) The galvanostatic cycling performance of bare WO_3, WO_3/C, and WO_3/WS_2 at a current density of 100 mA g^{-1} and the Coulombic efficiency (%), and (B) the specific capacities of WO_3, WO_3/C, and WO_3/WS_2 at various discharge currents of 0.1, 0.5, 0.7, 1, and 2 A g^{-1}

rapidly and cannot recover to initial specific capacitance values when returning to lower charge/discharge currents after cycling at high current rates. In contrast, when the test currents regularly return at a lower rate, at 0.1 A g^{-1}, the discharge capacities for WO_3/C and WO_3/WS_2 electrodes could recover to approximately the initial capacity values.

So, the specific capacity of the WO_3/C compound is greater than the WO_3/WS_2 and WO_3 electrodes in all cases. This can be attributed to efficient electron transport leading to a higher specific capacity thanks to the carbon coating compared to the other two electrodes over 50 charge–discharge cycles.

Furthermore, there may be an in situ transformation (during battery operation) of the WS_2 nanostructures. This has recently been highlighted in a research work,[9] in which an in situ modification of the WS_2 nanostructures resulted in lower cyclability and rate capability than the carbon coated electrode, but this behavior will be evaluated in future studies.

3.5.3 | EIS

In order to research the electrochemical performance of each electrode, the EIS was applied to WO_3, WO_3/C, and WO_3/WS_2 samples. These tests were taken before cycling and after 100 charge/discharge cycles within a frequency range from 10^4 to 0.01 Hz at 100 mA g^{-1}. As indicated in Nyquist plots (Figure 10), in the acquired spectra of

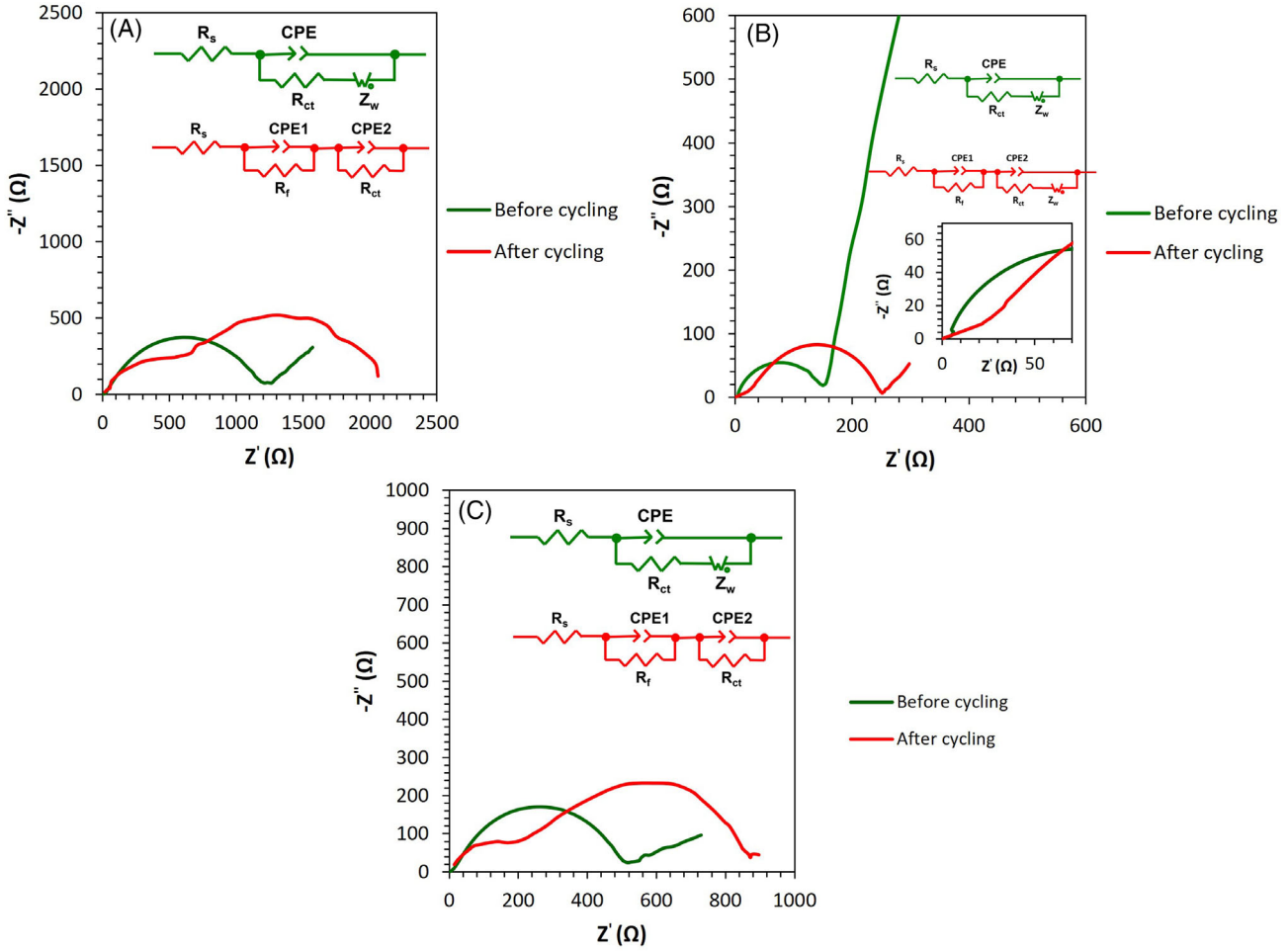

FIGURE 10 Nyquist impedance plots before and after the cycling of nanostructures based on (A) WO_3, (B) WO_3/C with an inset (a magnification of high frequency range), and (C) WO_3/WS_2 with a frequency range from 100 kHz to 10 mHz. The inserts are the equivalent circuits used to find the impedance parameters.

samples before cycling, a semicircle is found at high and medium frequencies, whereas at low frequencies, a sloping line can be seen. However, the spectra of samples after cycling change in the three electrodes but in different ways. In WO_3/C electrode, another semicircle appears, whereas in WO_3 and WO_3/WS_2 electrodes, in addition to the appearance of another semicircle, the inclined line disappears. The equivalents circuits that have been used for fitting the electrochemical impedance spectra are shown in Figure 10 insets, and the fitted impedance parameters are listed in Table 3.

Regarding the spectra obtained from the samples before cycling, the cutoff value of the semicircle at high frequencies on the *x*-axis (where Z' is represented) is associated with the ohmic resistance (R_s), which means the resistance of the electrolyte. The width of the semicircle is referred to the charge transfer resistance (R_{ct}), and the constant phase element symbolizes the electric capacitance of the double-layer in the electrode/electrolyte interface.[52] Moreover, the sloping line in the low-frequency zone (Z_w) is associated with Warburg impedance which, according to other investigations, is associated with Li-ion diffusion process.[53,54]

According to the spectra obtained after cycling, the diameter of the small semicircle (at the high frequency region) refers to the surface layer resistance, which is attributed to the lithium-ion diffusion across the nanostructures' surface and the creation of a passivation sheet on the nanostructures' surface.[55] The amplitude of the largest semicircle (in the low-frequency zone) is related to the charge transfer resistance, which is associated with the connection among the nanorods' edges or between the electrolyte/electrode interfaces.[13,56] Moreover finally, the sloping line that appears in WO_3/C electrode is related to Li-ion diffusion process.

The ohmic resistances (R_s) are very close for all samples, demonstrating that all nanostructures possess similar conductivity. Notably, the R_{ct} of WO_3/C nanostructures before and after cycling (147.5 and 343.9 Ω, respectively) was much smaller than the values obtained from WO_3 and WO_3/WS_2 samples. These results indicate that WO_3/C

TABLE 3 Impedance parameters and diffusion coefficients before and after cycling

		R_s (Ω)	R_{ct} (Ω)	CPE1 (C)	C1 (μF cm^{-2})	CPE2 (C)	C2 (μF cm^{-2})	D (cm^2 s^{-1})
WO_3	Before cycling	18.6	1242	$5.38\cdot10^{-5}$	13.6	–	–	$2.43\cdot10^{-14}$
	After cycling	13.68	1553	$3.75\cdot10^{-6}$	0.357	$4.43\cdot10^{-5}$	16.8	
WO_3/C	Before cycling	12.4	147.5	$2.21\cdot10^{-5}$	5.85	–	–	$5.18\cdot10^{-13}$
	After cycling	22.69	343.9	$9.5\cdot10^{-6}$	1.11	$1.79\cdot10^{-5}$	1.28	
WO_3/WS_2	Before cycling	15.24	541.9	$1.21\cdot10^{-4}$	26.03	–	–	$6.60\cdot10^{-14}$
	After cycling	17.41	695.3	$2.94\cdot10^{-5}$	0.174	$5.38\cdot10^{-5}$	13.2	

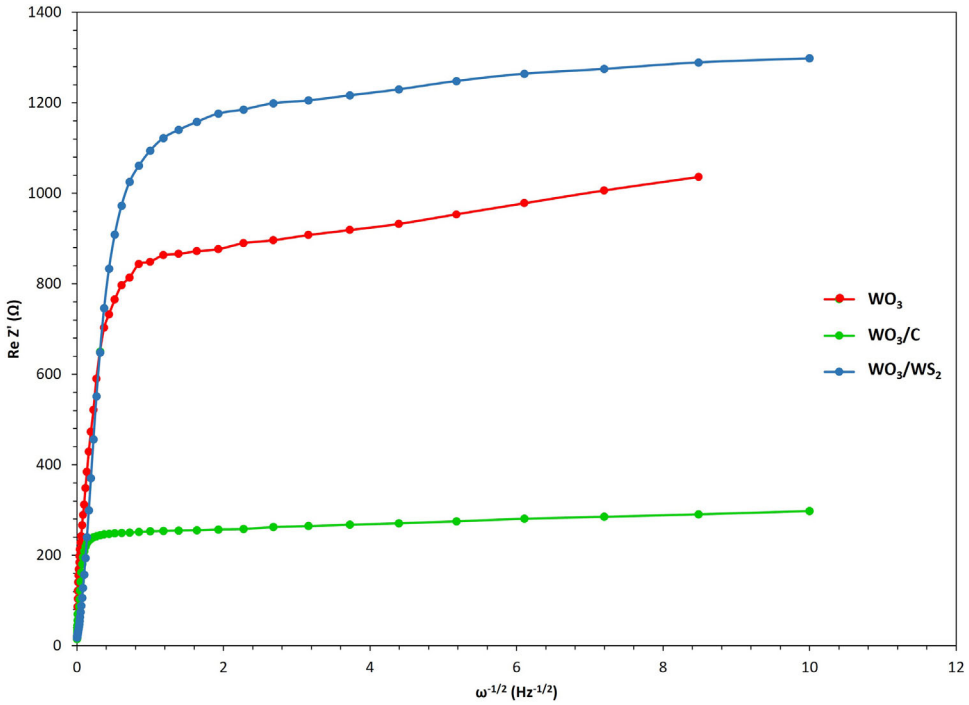

FIGURE 11 Randles circuits of WO_3, WO_3/C, and WO_3/WS_2

electrodes exhibit an improved electron transport capacity during the Li^+ insertion/de-insertion process and show shorter Li^+-ion diffusion path length.

Furthermore, Li^+ ion diffusion coefficients for the nanostructures have been obtained from the slope (k_w) of Randles circuits (Figure 11) by applying the following equation[57]:

$$k_w = \frac{R \cdot T}{n^2 \cdot F^2 \cdot A\sqrt{2}} \cdot \left(\frac{1}{D^{1/2} \cdot C^*}\right) \quad (5)$$

In which k_w is the slope from the Randles circuit, T is the temperature value (K), R corresponds to the gas constant, F is the Faraday constant, n is related to the charge transfer number, A is associated with the area of the electrode surface, C^* is ionic concentration, and D is the diffusion coefficient.[19,24] The Li^+ diffusion coefficients of WO_3, WO_3/C, and WO_3/WS_2 have been calculated, their values being 2.43×10^{-14}, 5.18×10^{-13}, and 6.6×10^{-14} cm^2 s^{-1}, respectively. These results show that the WO_3/C sample possesses the lowest Li^+ diffusion coefficient due to the higher amount of carbon, which favors the conductivity of the electrode. Consequently, it is acceptable to consider that the WO_3/C electrode is an anode material for which one may have hopes as to their use in lithium ion batteries.

4 | CONCLUSIONS

In summary, electrodes based on WO_3 nanostructures with some modifications in their composition have been synthesized using a simple method. The FE-SEM, HRTEM XPS, XRD, and Raman spectroscopy were applied to study the crystal structure and morphology of the samples.

FE-SEM and HRTEM images show that, in all cases, nanostructures were assembled in a well-defined morphology, such as nanorods, which is also advantageous to short ion length of diffusion to redox sites. However, the WO_3/WS_2 electrode shows a little difference in its morphology as these nanostructures are less defined and porous due to the thiourea deposition process.

With XPS analysis, XRD, and Raman spectra, we can conclude that a carbon film has been successfully deposited on the WO_3 nanostructures to yield a new electrode (WO_3/C) that is more conductive thanks to the presence of this element. In addition, with the sulfurization process, it has been possible to deposit sulfur, an element that improves the behavior of the electrodes, on the WO_3 nanostructures.

Galvanostatic tests and cyclic voltammograms (CV) were used to analyze the electrochemical performance of the WO_3/Li cell, and the WO_3/C electrode showed the highest discharge capacity to be 820 mA h g^{-1}. Furthermore, from the CV tests, it can be affirmed that these nanostructures do not display the irreversible reactions whereby they could lose cycling capacity.

Moreover, with EIS tests it has been revealed that WO_3/C nanostructures show a lower resistance to charge transfer and always preserve the component associated with the diffusion of Li^+, even after 100 cycles. Finally, the Li^+ diffusion coefficient is higher in this electrode, indicating a better cyclability capacity of the electrode.

These results indicate that WO_3/C nanostructures constitute a very promising anode material for lithium-ion batteries as they have useful properties for excellent behavior at LiB, comprising facile electron transference across carbon matrix, and better cyclability performance due to their morphology and composition.

ACKNOWLEDGMENTS

This work was supported by the AEI (PID2019-105844RB-I00/AEI/10.13039/501100011033) project. G. Roselló-Márquez is grateful to the UPV for the concession of a postdoctoral grant (PAID-10-21). M. Cifre-Herrando also thanks the Ministerio de Universidades for the concession of the predoctoral grant (FPU19/02466). Finally, the authors wish to thank the project co-funded by the FEDER operational program 2014–2020 of the Comunitat Valenciana (IDIFEDER/18/044) for the financial funding.

REFERENCES

1. Gu Z, Li H, Zhai T, Yang W, Xia Y, Ma Y, et al. Large-scale synthesis of single-crystal hexagonal tungsten trioxide nanowires and electrochemical lithium intercalation into the nanocrystals. J Solid State Chem. 2007;180(1):98–105.
2. Liu Z, Li P, Wan Q, Zhang D, Volinsky AA, Qu X. Low-temperature combustion synthesis of hexagonal $WO_3 \cdot 0.33H_2O$@C as anode material for lithium ion batteries. J Alloys Compd [Internet]. 2017;701:215–21. Available from: https://doi.org/10.1016/j.jallcom.2017.01.089
3. Lee SK, Kim H, Bang S, Myung ST, Sun YK. WO_3 nanowire/carbon nanotube interlayer as a chemical adsorption mediator for high-performance lithium-sulfur batteries. Molecules. 2021;26(2):377.
4. Srour H, Chancelier L, Bolimowska E, Gutel T, Mailley S, Rouault H, et al. Ionic liquid-based electrolytes for lithium-ion batteries: review of performances of various electrode systems. J Appl Electrochem. 2016;46(2):149–55.
5. Zhang X, Lei W, Ye X, Wang C, Lin B, Tang H, et al. A facile synthesis and characterization of graphene-like WS_2 nanosheets. Mater Lett [Internet]. 2015;159:399–402. Available from: https://doi.org/10.1016/j.matlet.2015.07.044
6. Kim GT, Jeong SS, Joost M, Rocca E, Winter M, Passerini S, et al. Use of natural binders and ionic liquid electrolytes for greener and safer lithium-ion batteries. J Power Sources [Internet]. 2011;196(4):2187–94. Available from: https://doi.org/10.1016/j.jpowsour.2010.09.080
7. Malini R, Uma U, Sheela T, Ganesan M, Renganathan NG. Conversion reactions: a new pathway to realise energy in lithium-ion battery—review. Ionics (Kiel). 2009;15(3):301–7.
8. Shiva K, Ramakrishna Matte HSS, Rajendra HB, Bhattacharyya AJ, Rao CNR. Employing synergistic interactions between few-layer WS_2 and reduced graphene oxide to improve lithium storage, cyclability and rate capability of Li-ion batteries. Nano Energy [Internet]. 2013;2(5):787–93. Available from: https://doi.org/10.1016/j.nanoen.2013.02.001
9. Zhang B, Luo C, Deng Y, Huang Z, Zhou G, Lv W, et al. Optimized catalytic WS_2–WO_3 heterostructure design for accelerated polysulfide conversion in lithium–sulfur batteries. Adv Energy Mater. 2020;10(15):2000091.
10. Liu Z, Li P, Dong Y, Wan Q, Zhai F, Volinsky AA, et al. Facile preparation of hexagonal $WO_3 \cdot 0.33H_2O$/C nanostructures and its electrochemical properties for lithium-ion batteries. Appl Surf Sci [Internet]. 2017;394:70–7. Available from: https://doi.org/10.1016/j.apsusc.2016.10.107
11. Chawla N, Bharti N, Singh S. Recent advances in non-flammable electrolytes for safer lithium-ion batteries. Batteries. 2019;5(1):1–25.
12. Huang K, Pan Q, Yang F, Ni S, Wei X, He D. Controllable synthesis of hexagonal WO_3 nanostructures and their application in lithium batteries. J Phys D Appl Phys. 2008;41(15):155417.
13. Park SK, Lee HJ, Lee MH, Park HS. Hierarchically structured reduced graphene oxide/WO_3 frameworks for an application into lithium ion battery anodes. Chem Eng J [Internet]. 2015;281:724–9. Available from: https://doi.org/10.1016/j.cej.2015.07.009
14. Yoon S, Woo SG, Jung KN, Song H. Conductive surface modification of cauliflower-like WO_3 and its electrochemical properties for lithium-ion batteries. J Alloys Compd [Internet]. 2014;613:187–92. Available from: https://doi.org/10.1016/j.jallcom.2014.06.010
15. NGUYEN TC, NGUYEN KA, PHUNG MN, NGO DX, LE TA, DO TD, et al. Ammonia gas sensing properties at low temperatures of nanocomposites of graphene oxide and tungsten oxide nanobricks. Vietnam J Sci Technol [Internet]. 2020;58(3):282. Available from: https://vjs.ac.vn/index.php/jst/article/view/14704

16. Li Y, Chang K, Tang H, Li B, Qin Y, Hou Y, et al. Preparation of oxygen-deficient WO_{3-x} nanosheets and their characterization as anode materials for high-performance Li-ion batteries. Electrochim Acta [Internet]. 2019;298:640–9. Available from: https://doi.org/10.1016/j.electacta.2018.12.137
17. Huang X. Separator technologies for lithium-ion batteries. J Solid State Electrochem. 2011;15(4):649–62.
18. Liu J, Zhang Z, Wang Z, Tang M, Li J, Yi J, et al. Flower-like WO_3/$CoWO_4$/Co nanostructures as high performance anode for lithium ion batteries. J Alloys Compd [Internet]. 2017;727:107–13. Available from: https://doi.org/10.1016/j.jallcom.2017.08.057
19. Hwang KS, Yoon TH, Lee CW, Son YS, Hwang JK. Discharge-charge characteristics and performance of Li/FeOOH(an) battery with PAN-based polymer electrolyte. J Power Sources. 1998;75(1):13–8.
20. Gao H, Yang S, Feng C, Wang J, Guo Z. Synthesis and electrochemical properties of nano WO_3/C for lithium ion batteries. ECS Trans. 2014;62(1):9–18.
21. Xu J, Li Y, Wang L, Cai Q, Li Q, Gao B, et al. High-energy lithium-ion hybrid supercapacitors composed of hierarchical urchin-like WO_3/C anodes and MOF-derived polyhedral hollow carbon cathodes. Nanoscale. 2016;8(37):16761–8.
22. Cao S, Zhao C, Han T, Peng L. The WO_3/WS_2 nanostructures: preparation, characterization and optical absorption properties. Physica E Low Dimens Syst Nanostruct [Internet]. 2016;81:235–9. Available from: https://doi.org/10.1016/j.physe.2016.03.027
23. Lim YR, Ko Y, Park J, Cho WI, Lim SA, Cha EH. Morphology-controlled WO_3 and WS_2 nanocrystals for improved cycling performance of lithium ion batteries. J Electrochem Sci Technol. 2019;10(1):89–97.
24. Hsieh Te C, Hsu SM, Lin JY, Teng H. Electrochemical capacitors based on graphene oxide sheets using different aqueous electrolytes. J Phys Chem C. 2011;115(25):12367–74.
25. Zou J, Liu C, Yang Z, Qi C, Wang X, Qiao Q, et al. Multilayer-Cake WS_2/C nanocomposite as a high-performance anode material for lithium-ion batteries: "regular" and "alternate". ChemElectroChem. 2017;4(9):2232–6.
26. Rosello-Marquez G, Fernandez-Domene RM, Sanchez-Tovar R, Cifre-Herrando M, Garcia-Anton J. Degradation of diazinon based on photoelectrocatalytic technique using enhanced WO_3 nanostructures: mechanism and pathway. J Environ Chem Eng. 2021;9(4).
27. Wang Y, Kong D, Shi W, Liu B, Sim GJ, Ge Q, et al. Ice templated free-standing hierarchically WS_2/CNT-rGO aerogel for high-performance rechargeable lithium and sodium ion batteries. Adv Energy Mater. 2016;6(21):1–9.
28. Duan X, Xiao S, Wang L, Huang H, Liu Y, Li Q, et al. Ionic liquid-modulated preparation of hexagonal tungsten trioxide mesocrystals for lithium-ion batteries. Nanoscale. 2015;7(6):2230–4.
29. Lian C, Xiao X, Chen Z, Liu Y, Zhao E, Wang D, et al. Preparation of hexagonal ultrathin WO_3 nano-ribbons and their electrochemical performance as an anode material in lithium ion batteries. Nano Res. 2016;9(2):435–41.
30. Li WJ, Fu ZW. Nanostructured WO_3 thin film as a new anode material for lithium-ion batteries. Appl Surf Sci. 2010;256(8):2447–52.
31. Xing LL, Huang KJ, Fang LX. Preparation of layered graphene and tungsten oxide hybrids for enhanced performance supercapacitors. Dalton Trans. 2016;45(43):17439–46.
32. Yang J, Xu L, Yan S, Zheng W. Formation of tungsten trioxide with hierarchical architectures arranged by tiny nanorods for lithium ion batteries. RSC Adv. 2016;6(22):18071–6.
33. Pang Q, Gao Y, Zhao Y, Ju Y, Qiu H, Wei Y, et al. Improved lithium-ion and sodium-ion storage properties from few-layered WS_2 nanosheets embedded in a mesoporous CMK-3 matrix. Chemistry—A Eur J. 2017;23(29):7074–80.
34. Zhou L, Yan S, Pan L, Wang X, Wang Y, Shi Y. A scalable sulfuration of WS_2 to improve cyclability and capability of lithium-ion batteries. Nano Res. 2016;9(3):857–65.
35. Sasidharan M, Gunawardhana N, Yoshio M, Nakashima K. WO_3 hollow nanospheres for high-lithium storage capacity and good cyclability. Nano Energy [Internet]. 2012;1(3):503–8. Available from: https://doi.org/10.1016/j.nanoen.2012.03.003
36. Tong H, Xu Y, Cheng X, Zhang X, Gao S, Zhao H, et al. One-pot solvothermal synthesis of hierarchical WO_3 hollow microspheres with superior lithium ion battery anode performance. Electrochim Acta [Internet]. 2016;210:147–54. Available from: https://doi.org/10.1016/j.electacta.2016.05.154
37. Jo C, Lim WG, Dao AH, Kim S, Kim S, Yoon S, et al. Tracking the confinement effect of highly dispersive carbon in a tungsten oxide/carbon nanocomposite: conversion anode materials in lithium ion batteries. J Mater Chem A. 2017;5(47):24782–9.
38. Bao K, Mao W, Liu G, Ye L, Xie H, Ji S, et al. Preparation and electrochemical characterization of ultrathin WO_{3-x}/C nanosheets as anode materials in lithium ion batteries. Nano Res. 2017;10(6):1903–11.
39. Siddique F, Fareed S, Jamil A, Afsar MF, Rafiq MA, Sher F. Synthesis of randomly oriented self-assembled WO_3 and WO_3-WS_2 nanoplates for selective oxygen sensing. J Aust Ceram Soc. 2021;57(4):1231–40.
40. Muzaffar T, Khosa RY, Iftikhar U, Obodo RM, Sajjad S, Usman M. Synthesis and characterization of WO_3/GO nanocomposites for antimicrobial properties. J Cluster Sci [Internet]. 2021;2:1987–96. Available from: https://doi.org/10.1007/s10876-021-02116-2
41. Zeng F, Ren Y, Chen L, Yang Y, Li Q, Gu G. Hierarchical sandwich-type tungsten trioxide nanoplatelets/graphene anode for high-performance lithium-ion batteries with long cycle life. Electrochim Acta [Internet]. 2016;190:964–71. Available from: https://doi.org/10.1016/j.electacta.2015.12.109
42. Wang P, Cheng Z, Lv G, Qu L, Zhao Y. Coupling interconnected MoO_3/WO_3 nanosheets with a graphene framework as a highly efficient anode for lithium-ion batteries. Nanoscale. 2018;10(1):396–402.
43. Badiezadeh F, Kimiagar S. Modified WO_3 nanosheets by N-GO nanocomposites to form NO_2 sensor. J Exp Nanosci [Internet]. 2021;16(1):145–59. Available from: https://doi.org/10.1080/17458080.2021.1922670
44. Liu Y, Li W, Li J, Yang Y, Chen Q. Enhancing photoelectrochemical performance with a bilayer-structured film consisting of graphene-WO_3 nanocrystals and WO_3 vertically plate-like arrays as photoanodes. RSC Adv. 2014;4(7):3219–25.
45. Liu F, Kim JG, Lee CW, Im JS. A mesoporous WO 3-X/graphene composite as a high-performance Li-ion battery anode. Appl Surf Sci [Internet]. 2014;316(1):604–9. Available from: https://doi.org/10.1016/j.apsusc.2014.07.189
46. Li P, Li X, Zhao Z, Wang M, Fox T, Zhang Q, et al. Correlations among structure, composition and electrochemical performances of WO_3 anode materials for lithium ion batteries. Electrochim Acta. 2016;192:148–57.

47. Li G, Li Z, Zhang B, Lin Z. Developments of electrolyte systems for lithium-sulfur batteries: a review. Front Energy Res. 2015;3(FEB):1–12.
48. Tang ZK, Tse JS, Liu LM. Unusual Li-ion transfer mechanism in liquid electrolytes: a first-principles study. J Phys Chem Lett. 2016;7(22):4795–801.
49. Rui X, Tan H, Yan Q. Nanostructured metal sulfides for energy storage. Nanoscale. 2014;6(17):9889–924.
50. Eftekhari A. Tungsten dichalcogenides (WS_2, WSe_2, and WTe_2): materials chemistry and applications. J Mater Chem A. 2017;5(35):18299–325.
51. Gu X, Wu F, Lei B, Wang J, Chen Z, Xie K, et al. Three-dimensional nitrogen-doped graphene frameworks anchored with bamboo-like tungsten oxide nanorods as high performance anode materials for lithium ion batteries. J Power Sources [Internet]. 2016;320:231–8. Available from: https://doi.org/10.1016/j.jpowsour.2016.04.103
52. Yang W, Wang J, Si C, Peng Z, Zhang Z. Tungsten diselenide nanoplates as advanced lithium/sodium ion electrode materials with different storage mechanisms. Nano Res. 2017;10(8):2584–98.
53. Zheng M, Tang H, Li L, Hu Q, Zhang L, Xue H, et al. Hierarchically nanostructured transition metal oxides for lithium-ion batteries. Adv Sci. 2018;5(3):1700592.
54. Faraji M, Hassanzadeh A, Mohseni M. Interlaced WO_3-carbon nanotube nanocomposite electrodeposited on graphite as a positive electrode in vanadium redox flow battery. Thin Solid Films [Internet]. 2017;642(September):188–94. Available from: https://doi.org/10.1016/j.tsf.2017.09.044
55. Zhou S, Chen J, Gan L, Zhang Q, Zheng Z, Li H, et al. Scalable production of self-supported WS_2/CNFs by electrospinning as the anode for high-performance lithium-ion batteries. Sci Bull. 2016;61(3):227–35.
56. Xu H, Wu C, Wei X, Gao S. Hierarchically porous carbon materials with controllable proportion of micropore area by dual-activator synthesis for high-performance supercapacitors. J Mater Chem A. 2018;6(31):15340–7.
57. Wu X, Yao S. Flexible electrode materials based on WO_3 nanotube bundles for high performance energy storage devices. Nano Energy [Internet]. 2017;42(September):143–50. Available from: https://doi.org/10.1016/j.nanoen.2017.10.058

How to cite this article: Roselló-Márquez G, García-García DM, Cifre-Herrando M, Blasco-Tamarit E, García-Antón J. Facile preparation of electrodes based on WO_3 nanostructures modified with C and S used as anode materials for Li-ion batteries. J Am Ceram Soc. 2023;106:2550–2566. https://doi.org/10.1111/jace.18910